70th International Astronautical Congress (IAC), Washington D.C, United States, 21-25 October 2019.

IAC-19.A6.3.11

Assessing Debris Strikes in Spacecraft Telemetry: Development and Comparison of Various Techniques

Anne Aryadne Bennett[a]*, Hanspeter Schaub[b], Russell Carpenter[c]

[a] *Graduate Researcher, University of Colorado, 3775 Discovery Dr, Boulder, CO 80303.* anne.a.bennett@colorado.edu
Mission Systems Engineer, Northrop Grumman Innovation Systems, 45101 Warp Dr, Dulles, VA, 20166.
[b] *Glenn L. Murphy Endowed Chair, Professor of Smead Aerospace Engineering Sciences Department, University of Colorado, 3775 Discovery Dr, Boulder, CO 80303.*, hanspeter.schaub@colorado.edu
[c] *Deputy Project Manager/Technical, NASA Space Science Mission Operations, NASA Goddard Space Flight Center, Greenbelt, MD, 20771*, russell.carpenter@nasa.gov
* Corresponding Author

Abstract

Debris strikes on operational spacecraft are becoming more common due to increasing numbers of space objects. Sample return missions indicate hundreds of minor strikes, but rigorous analysis is often only performed when a strike causes an anomaly in spacecraft performance. Developing techniques to identify and assess minor strikes that do not immediately cause anomalous behavior can help to validate models for debris populations, perform risk assessments, and aid in the attribution of future anomalies. This study introduces debris strikes to a spacecraft dynamics simulation and assesses the effect on spacecraft telemetry. Various signal processing and change detection techniques are used to identify strikes in noisy telemetry and estimate strike parameters. Matched filter wavelets are developed to identify the effects on state telemetry, where errors are autonomously corrected by the spacecraft attitude control system. A bank of matched filters is used to estimate the parameters of the strike based on *a priori* knowledge of the spacecraft's response characteristics. A sequential probability ratio test is used to highlight abrupt changes in the spacecraft's angular momentum. Monte-Carlo analyses are conducted to characterize the performance of these algorithms. The results of the various techniques are compared in terms of correctly identifying the debris strikes and accurately estimating the strike parameters. Developing the capability to catalog and characterize minor debris strikes allows any spacecraft to be used as an *in situ* debris sensor.
Keywords: Debris strike, perturbation, attitude, telemetry, matched filter, change detection.

1. Introduction

The population of trackable fragmentation debris has more than doubled in the past 25 years [1]. This is especially concerning because while trackable debris can be avoided by maneuvering satellites, most fragmentation events also release clouds of debris too small to track. The Space Surveillance Network (SSN) tracks debris down to around 10 cm in LEO and 70 cm in GEO [2], but a 1 cm piece of debris can cause catastrophic damage to a spacecraft if it hits a sensitive component [3, 4]. As of January 2019, there are approximately 34,000 debris objects greater than 10 cm in orbit; but there are approximately 900,000 objects between 1 cm and 10 cm [5]. Therefore, well under 10% of the potentially hazardous debris population is tracked.

However, there have been some indications that current debris models may be overly conservative. This is burdensome for ongoing programs as it makes it difficult to show compliance with debris mitigation standards. A recent study by the NASA Engineering and Safety Council (NESC) found that NASA's debris model consistently overpredicted the likelihood of failure across several case studies [6].

Two recent events illustrate the potential effects of strikes from untracked debris. In August of 2016, the Sentinel-1A spacecraft experienced an anomaly consisting of an abrupt attitude perturbation (Fig. 1) coupled with a slight orbit change and simultaneous decrease in solar power output. On-board cameras confirmed a debris strike on the solar array. However, the solar array strike was non-catastrophic and operations continued nominally [7]. More recently, in April 2019, Intelsat-29e experienced an abrupt anomaly resulting in a fuel leak and shed debris, culminating in the total loss of the satellite. The failure review board concluded that the anomaly was caused by either a particle strike or an electrostatic discharge event coupled with an existing harness flaw [8].

Taking these facts together, there is a significant population of untracked hazardous debris with the potential to grow rapidly. There is reason for concern about the

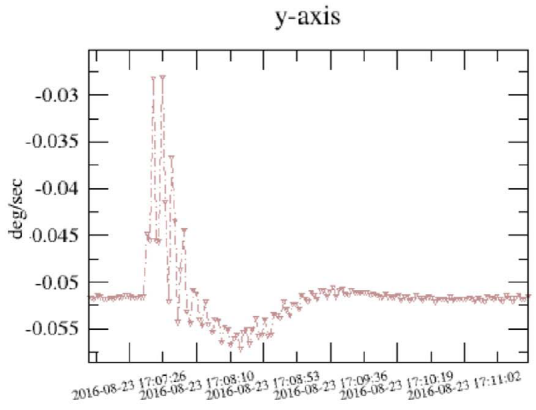

Fig. 1: Rate gyro measurements from Sentinel-1A anomaly show an abrupt spike in rate which is corrected by the attitude control system (ACS) [7]

accuracy of debris models, but *in situ* measurements are difficult to obtain, especially for the larger and potentially hazardous untracked population. This paper investigates an innovative method to obtain *in situ* measurements of debris that is too small to track but still large enough to effect a spacecraft. It accomplishes this by applying digital signal processing (DSP) and change detection (CD) techniques to spacecraft attitude control system (ACS) telemetry to identify and assess subtle indicators of debris strikes.

Most prior work on detecting debris strikes involves the assessment of a specific event or mission. Similar to the Sentinel-1A anomaly, a recent strike on NASA's Magnetospheric Multiscale (MMS) constellation caused anomalous behavior but was fully recoverable [9]. The strike was observed as a loss of one shunt resistor and a spike in the plasma coupled with a dynamic event. On the spin-stabilized MMS spacecraft the dynamic event caused ringing in the accelerometer telemetry, excitation of boom vibration resulting in atypical nutation of the transverse rotation rates, and temporary loss of valid startracker attitude fix. In both the Sentinel-1A and the MMS events the strike caused anomalous (but recoverable) behavior which resulted in a thorough investigation of the telemetry. A smaller strike with more subtle indicators may go unnoticed.

There have been several papers on the results of sample return missions [10, 11] or on custom hardware which is flown specifically to detect debris [12, 13]. There are a handful of studies which use data from non-purpose-built hardware to detect impacts on orbit. The bulk of these detect dust impacts on antennas [14]. However, the dust impacts have masses around 10^{-11} g or less so the ability of this population to harm satellites is limited. This paper investigates strikes large enough to perturb the spacecraft dynamics, since the hazard is from debris pieces large enough to cause damage if impacting sensitive components.

Some key work has been done by ExoAnalytic Solutions on detecting 'momentum impulse transfer events' on GEO spacecraft using their global telescope network. They have proven a capability to detect orbit perturbations with in-track velocity changes of 0.2 - 10 mm/s [15]. Some of these are explained with rigorous high-fidelity modeling of solar radiation pressure, but others remain unexplained and could be caused by on-board systems or, potentially, debris impacts.

A similar concept is discussed in a recent NESC report evaluating risk predictions with on-orbit assets [6]. This report compares the predicted vs. reported failures for ISS radiators and pressurized modules and for three LEO satellite systems. For one LEO constellation, seven events had been observed where satellites experienced sudden unexpected movements thought to be caused by debris. These movements consisted of abrupt changes in satellite mean altitude or rotation rates. One of the recommendations of the NESC report is to collect data on satellite orbital perturbations and momentum changes. This paper develops algorithms to accomplish that using DSP/CD techniques to enhance the ability to identify subtle strikes.

While prior work focuses on specific events, this paper develops methods to detect strikes which may not otherwise be observed. It leverages established techniques from other fields to aid in solving the untrackable debris problem. In approaching the problem from the reverse direction, identifying subtle strikes instead of responding to anomalous behaviors as they occur, it allows spacecraft operators and the debris community to proactively improve models and methods for assessing debris risks and attributing anomalies.

A spacecraft dynamics simulation is used to model the effect of debris strikes on ACS telemetry. The numerical simulation models a 3-axis controlled rigid-body spacecraft with four reaction wheels maintaining pointing along a reference trajectory (Section 2.1). Debris strikes are applied to the simulation per Section 3.1, while state noise and measurement noise obfuscate the spacecraft's response to the strikes. Section 3.2 investigates the ability of matched filters to identify the 'signals' produced in spacecraft state telemetry during a debris strike. This includes developing thresholds for detection (Section 3.2.2), developing methods to estimate strike parameters (Section 3.2.3), and using a Monte-Carlo analysis to assess algorithm performance (Section 3.2.4). Section 3.3 applies CD techniques to the momentum telemetry, which exhibits lasting changes when a debris strike imparts a change in the spacecraft's inertial angular momentum.

2. Methods for Simulation and Telemetry Processing

2.1 Spacecraft Simulation

A numerical spacecraft dynamics simulation is used to investigate a spacecraft's response to debris strikes. The

simulated spacecraft is configured as a rigid-body 3-axis controlled inertially-pointing GEO satellite with four reaction wheels (RWs). The state vector consists of the spacecraft's attitude and rate along with the rotation speeds of the four reaction wheels. A Runge-Kutta fourth-order integrator is used to integrate the equations of motion given in Equations (1), (2), and (3) [16]. Note that Equations (2) and (3) must be solved simultaneously.

$$\dot{\boldsymbol{q}} = \frac{1}{2}\begin{bmatrix} -q_1 & -q_2 & -q_3 \\ q_0 & -q_3 & q_2 \\ q_3 & q_0 & -q_1 \\ -q_2 & q_1 & q_0 \end{bmatrix}\boldsymbol{\omega} \tag{1}$$

$$[I_{\text{sc}}]\dot{\boldsymbol{\omega}} + I_{ws}[G_s]\dot{\boldsymbol{\Omega}} = -[\tilde{\boldsymbol{\omega}}][I_{\text{sc}}]\boldsymbol{\omega} + \boldsymbol{L}_{\text{ext}} - \sum_{i=1}^{N}[\hat{\boldsymbol{g}}_{ti}I_{ws}\Omega_i\hat{\boldsymbol{g}}_{gi}^T\boldsymbol{\omega} - \hat{\boldsymbol{g}}_{gi}I_{ws}\Omega_i\hat{\boldsymbol{g}}_{ti}^T\boldsymbol{\omega}] \tag{2}$$

$$I_{ws}[G_s]^T\dot{\boldsymbol{\omega}} + I_{ws}[I_{N\times N}]\dot{\boldsymbol{\Omega}} = \boldsymbol{u}_s \tag{3}$$

The spacecraft's rotation rate, $\boldsymbol{\omega}$, is the rate of the body frame relative to an inertial frame, and is expressed in body frame coordinates. The attitude quaternion of the body relative to inertial is $\boldsymbol{q}$, and $\boldsymbol{\Omega}$ is an $N \times 1$ matrix of wheel speeds for N reaction wheels. The external torque applied by the debris strike is $\boldsymbol{L}_{\text{ext}}$ while $\hat{\boldsymbol{g}}_{si}$ is the unit vector of the spin axis of the ith reaction wheel. The transverse directions are $\hat{\boldsymbol{g}}_{ti}$ and $\hat{\boldsymbol{g}}_{gi}$, and the $[G_s]$ matrix is defined as $[G_s] = [\hat{\boldsymbol{g}}_{s1}...\hat{\boldsymbol{g}}_{sN}]$. The spacecraft inertia (with reaction wheels included) is given as $[I_{\text{sc}}]$, and the spin-axis inertia if each reaction wheel is I_{ws}. An identity matrix is denoted as $[I_{N\times N}]$, and the applied control torques for each reaction wheel are specified in $\boldsymbol{u}_s$. These control torques are calculated as shown in Equation (4) to apply a desired torque, $\boldsymbol{L}_{\text{des}}$, which is calculated per Equation (5).

$$\boldsymbol{u}_s = [G_s]^T([G_s][G_s]^T)^{-1}\boldsymbol{L}_{\text{des}} \tag{4}$$

Note that the Modified Rodrigues Parameters (MRPs, $\boldsymbol{\sigma}$) are used as the attitude coordinate for the control law and represent the attitude error between the current body frame and the desired reference frame. Similarly, $\delta\boldsymbol{\omega}$ represents the difference between $\boldsymbol{\omega}$ and the desired reference angular velocity, $\boldsymbol{\omega}_r$ [16].

$$\boldsymbol{L}_{\text{des}} = K\boldsymbol{\sigma} + [P]\delta\boldsymbol{\omega} - [\tilde{\boldsymbol{\omega}}][I_{\text{sc}}]\boldsymbol{\omega} - [I_{\text{sc}}](\dot{\boldsymbol{\omega}}_r - \boldsymbol{\omega}\times\boldsymbol{\omega}_r) \tag{5}$$

The proportional control gain on attitude error is denoted as K, and $[P]$ must be a positive definite matrix to guarantee stability via Lyapunov functions.

State noise is added to the system at each timestep in a Gaussian random walk. Gaussian measurement noise is added to $\boldsymbol{\omega}$ and $\boldsymbol{\sigma}$ when calculating the control torques and is also added to the torque command. The state is saved throughout the simulation and then truncated to a lower rate to represent downlinked telemetry. Gaussian measurement noise is added to this telemetry prior to processing. Table 1 contains the parameters used in this simulation. All noise is zero mean.

The spacecraft's inertial angular momentum is calculated from the noisy state telemetry via

$${}^{\mathcal{B}}\boldsymbol{H} = [I_{\text{sc}}]\boldsymbol{\omega} + \sum_{i=1}^{N}[BW]_i\begin{bmatrix} I_{ws}\Omega_i \\ 0 \\ 0 \end{bmatrix} \tag{6}$$

$${}^{\mathcal{N}}\boldsymbol{H} = [NB]\,{}^{\mathcal{B}}\boldsymbol{H} \tag{7}$$

where ${}^{\mathcal{B}}\boldsymbol{H}$ is the spacecraft angular momentum in the body-fixed frame, $[BW]_i$ is the direction cosine matrix to go from the ith wheel's coordinate frame to the body frame, $[NB]$ is the direction cosine matrix to go from the body frame to the inertial frame, and ${}^{\mathcal{N}}\boldsymbol{H}$ is the spacecraft's inertial angular momentum. Note that the momentum telemetry does not have any noise added to it, but it incorporates the noise from the attitude telemetry, rate telemetry, and wheel speed telemetry.

Table 1: Parameters used in spacecraft dynamics simulation

Parameter	Value	Unit
S/C Inertia$_{xx}$	3000	kg.m^2
S/C Inertia$_{yy}$	2500	kg.m^2
S/C Inertia$_{zz}$	3500	kg.m^2
RW Inertia	0.16	kg.m^2
RW max torque	0.2	N.m
RW 1 pointing vector	[1, 0, 0]	-
RW 2 pointing vector	[0, 1, 0]	-
RW 3 pointing vector	[0, 0, 1]	-
RW 4 pointing vector	[1, 1, 1]	-
State noise in attitude	σ=1E-8	-
State noise in rate	σ=1E-8	rad/s
Meas. noise in attitude sim	σ=1E-6	-
Meas. noise in rate sim	σ=1E-6	rad/s
Noise in applied torque	σ=0.001	N.m
Meas. noise in attitude tlm.	σ=7E-5	-
Meas. noise in rate tlm.	σ=2E-4	rad/s
Meas. noise in RW speed tlm.	σ=0.25	rad/s

2.2 Digital Signal Processing Techniques

Matched filters are used on the rate and attitude telemetry to identify debris strikes, since the spacecraft's dynamic response to the strike produces a known 'signal' in the telemetry. A matched filter will maximize the output signal-to-noise ratio (SNR) for a known signal in independent and identically distributed Gaussian noise.

A matched filter functions by taking a known wavelet (the anticipated signal) and cross-correlating it with a se-

quence of measurements. The filter output will increase when the signal is present in the noise, as shown in Figure 5 [17].

To determine the threshold for detecting a debris strike based on filter output, a receiver operating characteristic (ROC) curve is developed empirically and a desired probability of false alarm, α, is selected. The ROC curve shows the probability of false alarm (P_{FA}) vs. the probability of detection (P_D), which is based on two probability density functions (pdfs) (Figure 2(a)). The first pdf characterizes the filter output when no debris strike is present (i.e, the null hypothesis, $\mathcal{H}_o$). The second pdf characterizes the filter's peak when a certain debris strike is present ($\mathcal{H}_1$). Note that in order to decrease the P_{FA} the threshold is moved to the right, but that necessarily decreases the P_D for that strike and increases the probability of a missed detection, P_{MD}. Also, while Gaussian pdfs are shown in the figure they will only generate accurate thresholds if the data is Gaussian. Therefore, the distribution of the data should always be checked and appropriate pdfs selected before applying this method.

From the P_{FA} and P_D the ROC curves in Figure 2(b) are developed. A desired P_{FA} is selected, and the slope of the ROC curve at the point where $P_{FA} = \alpha$ is the threshold for the likelihood ratio test, τ_{thresh}. The likelihood ratio test, $\mathcal{L}$, is also based on the two pdfs of the filter output where

$$\mathcal{L}(\mathbf{y}) = \frac{\mathrm{p}\left(\mathbf{y}|\mathcal{H}_1\right)}{\mathrm{p}\left(\mathbf{y}|\mathcal{H}_0\right)} \underset{\mathcal{H}_o}{\overset{\mathcal{H}_1}{\gtrless}} \tau_{\text{thresh}} \tag{8}$$

Where $\mathrm{p}\left(\mathbf{y}|\mathcal{H}_i\right)$ is the probability of $\mathbf{y}$ given hypothesis $\mathcal{H}_i$. The resulting $\mathcal{L}(\mathbf{y})$ is compared to the threshold τ_{thresh} from the ROC curve and the appropriate hypothesis is selected. This threshold is mapped back to the filter output by finding the point at which τ_{thresh} intersects the $\mathcal{L}(\mathbf{y})$ line and choosing the corresponding $\mathbf{y}_{\text{thresh}}$ as the filter output threshold (Figure 2(c)).

$$\mathcal{L}(\mathbf{y}_{\text{thresh}}) = \tau_{\text{thresh}} \tag{9}$$

Note that the log of the likelihood ratio test (LLRT) is plotted along with the log of the threshold since the numbers become large. Under the Neyman-Pearson Lemma, this is the most powerful test that maximizes P_D under the constraint $P_{FA} = \alpha$ [18]. For the purposes of debris strike detection the filter output is compared to the threshold $\mathbf{y}_{\text{thresh}}$. If the filter output is above this threshold then a strike is declared and the strike parameters are estimated.

2.3 Change Detection Techniques

The inertial angular momentum of a spacecraft is quiescent in the absence of external forces, but a debris strike imparts an abrupt change in the momentum. Three techniques for detecting changes in quiescent but noisy data are applied to the spacecraft momentum: a simple summation filter, a more refined cumulative sum (CUSUM) sequential probability ratio test (SPRT), and a Shiryaev SPRT.

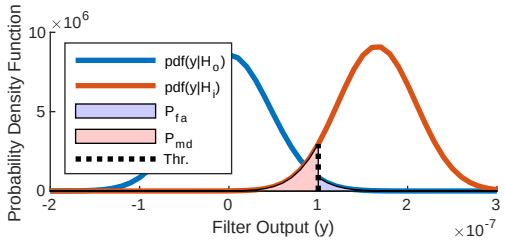

(a) Pdfs of Attitude Filter Output

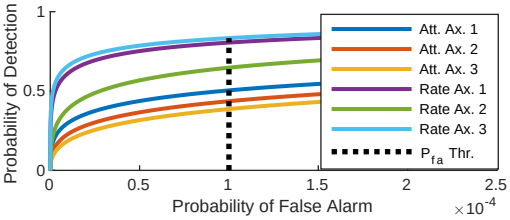

(b) ROC Curves and P_{fa} Threshold

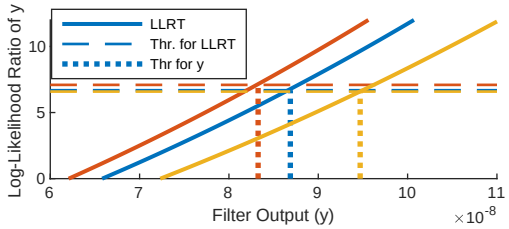

(c) Log-LRT and Thresholds from Slope of ROC

Fig. 2: Development of filter thresholds via ROC curve and LRT

The simple summation filter detects changes by adding the sum of all datapoints after zeroing the data to the expected average. For zero-mean noise, this sum trends to zero over time so that a value above a certain threshold indicates that a fault (or change) has occurred.

The CUSUM algorithm utilizes the log of the likelihood ratio test from Equation (8), summed sequentially to give the test statistic S_n [17].

$$S_n = \sum_{k=1}^{n} \ln(\mathcal{L}(\mathbf{y})) \tag{10}$$

The parameter S_n trends negative when the samples, as a whole, are more likely to be from $\mathcal{H}_o$ than $\mathcal{H}_1$, and trends positive when they are more likely from $\mathcal{H}_1$. This change in drift is detected through

$$W_n = S_n - \min_{0 \leqslant k < n} S_k \tag{11}$$

where W_n stays close to zero while S_n trends downward, then grows if it trends upward.

The multi-hypothesis Shiryaev SPRT is implemented for m alternative hypotheses per Malladi and Speyer [19].

They define

$$\phi_{ki} = F_{ki} + \tilde{p_i} \cdot (1 - F_{ki}) \tag{12}$$

Where F_{ki} is the cumulative distribution function (CDF) expressing the probability that, at datapoint k, hypothesis i is true. $\tilde{p_i}$ is the *a priori* probability that a transition to hypothesis i occurs. $F_{k+1,i}$ is computed recursively given each new datapoint x_{k+1} via where $f_i(x_{k+1})$ is the pdf of x_{k+1} given hypothesis i

$$F_{k+1,i} = \frac{\phi_{ki} \cdot f_i(x_{k+1})}{\sum_{j=1}^{m} \phi_{kj} \cdot f_j(x_{k+1})} \tag{13}$$

The CDFs are initialized to F_{oi}, which is the probability that a transition to hypothesis i has already occurred.

3. Algorithm Development

3.1 Applying Debris Strike to Simulation

The debris strike is applied to the spacecraft attitude dynamics simulation as a brief torque $\boldsymbol{L}$, computed as follows. The net change in momentum imparted by the debris strike is denoted as $\boldsymbol{H}_{\text{strike}}$ where $\boldsymbol{R}_{d/s}$ is the location of the strike relative to the spacecraft center of mass, m_d is the mass of the debris, and $\boldsymbol{V}_{d/s}$ is the velocity of the debris relative to the spacecraft.

$$\boldsymbol{H}_{\text{strike}} = \boldsymbol{R}_{d/s} \times m_d \boldsymbol{V}_{d/s} \tag{14}$$

$$\boldsymbol{H}_{\text{strike}} = \int \boldsymbol{L} \, \mathrm{d}t \tag{15}$$

The torque, $\boldsymbol{L}$, is applied in the simulation for one time step, and the torque magnitude in each axis is calculated such that the total change in momentum, $\boldsymbol{H}_{\text{strike}}$, is as specified in the problem setup.

For convenience, the traded debris strike variables are the direction of $\boldsymbol{H}_{\text{strike}}$ and the mass of the debris. The velocity of the debris is fixed at 8 km/s normal to $\boldsymbol{R}_{d/s}$, which is 1 m. The mass of the debris is traded to investigate different magnitudes of debris strike, and is generally between 1 and 100 mg. Note that in reality the velocity of debris would be dependent on the debris (or micrometeoroid) population it originates from, and the strike could be anywhere on the spacecraft. The variables are fixed for simplicity and clarity since this work focuses on modeling the effect on the spacecraft and developing detection methodologies, not on modeling the debris population.

It is important to note that a strike which breaks through a solar array will impart less momentum than the total relative momentum of the debris, while a strike which breaks up on the surface will cause a plume of ejecta in the reverse direction which increases the imparted momentum by a factor of two or more [20]. While these effects are critical for accurately modeling impact events, they are not captured in this work as the emphasis is on detection techniques, not debris population modeling. When these techniques are applied to on-orbit telemetry and used to estimate parameters in real debris strikes, these effects must be accounted for.

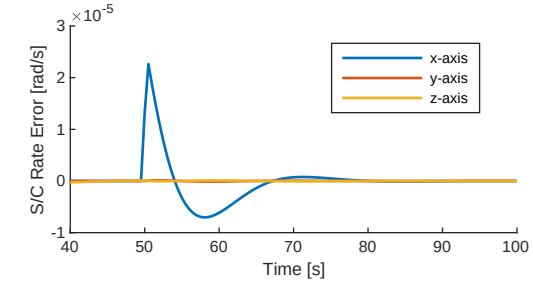

(a) Rate Telemetry

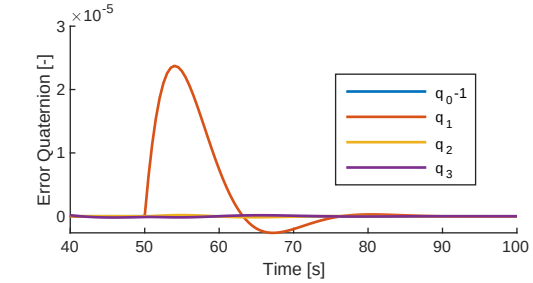

(b) Attitude Telemetry

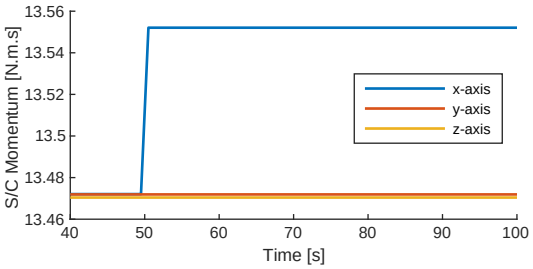

(c) Momentum Telemetry

Fig. 3: Response of spacecraft to simulated debris strike (10 mg at 8 km/s, 1 m from CoG, applied at t=50 s. ΔH = 0.08 N.m.s). Note similarity between rate telemetry and Sentinel-1A telemetry (Fig. 1)

When a debris strike is applied to a truth simulation with no noise, the results are as shown in Figure 3. The strike induces a rotation in the spacecraft which is corrected by the attitude control system. It manifests as a spike in the spacecraft rate, a drift and correction in the spacecraft attitude, and a net increase spacecraft momentum.

3.2 Matched Filter Development

The following sections outline the development and implementation of matched filters for detecting debris strikes using this spacecraft dynamics simulation.

3.2.1 Develop Filters to Identify Strikes

The truth simulation is used to develop matched filters for the spacecraft rate and attitude. To obtain the strike detection wavelet the simulation is run with the largest debris strike that does not saturate the RW torque. Since the frequency of the spacecraft's response is the same when correcting any strike too small to saturate the RWs, this largest wavelet envelopes the response of the spacecraft to smaller strikes. A filter with this wavelet produces a comparable SNR to a wavelet that matches the size of the strike, and thus only one detection wavelet needs to be run on each axis. A strike which saturates the wheel torques is detectable without a closely matched wavelet due to its large magnitude. Figure 5 shows the wavelet developed for the spacecraft rate applied to noisy telemetry, with the filter output showing a spike at the corresponding time.

To develop wavelets for a real spacecraft, the flatsat or an alternate dynamics simulation can be used to develop initial wavelets. Once the satellite is in orbit, the spacecraft's response to other momentum-changing events can be used to tune the wavelets. For example, a spacecraft's response to a slight angular momentum imparted during small maneuver has similar characteristics to the response to a debris strike. Figure 4 shows some telemetry from NASA's Solar Dynamics Observatory (SDO) recovering its attitude after a maneuver.

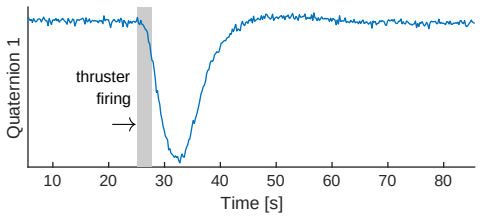

(a) Attitude Telemetry

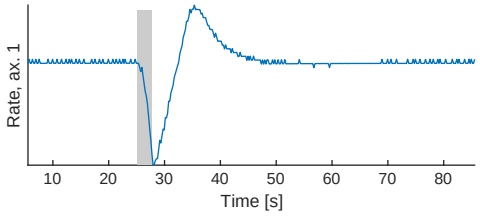

(b) Rate Telemetry

Fig. 4: Example of spacecraft correction after a small maneuver imparts a slight rotation. Note similarities to simulated debris strike response.

Note that the attitude wavelets are only run on the vector components of the error quaternion, since the scalar component will always be close to one for small errors. Under the small angle approximation, the scalar component will remain near one but the vector components will

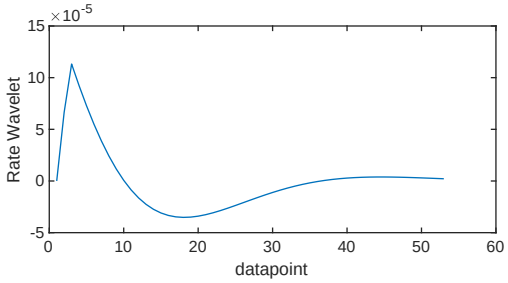

(a) Matched Filter Wavelet

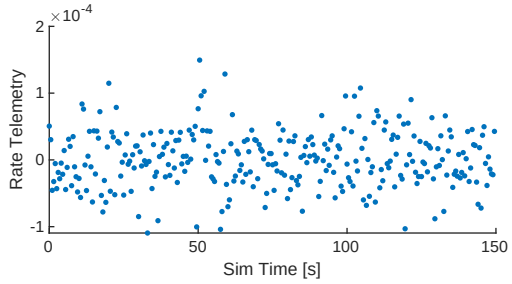

(b) Rate Telemetry

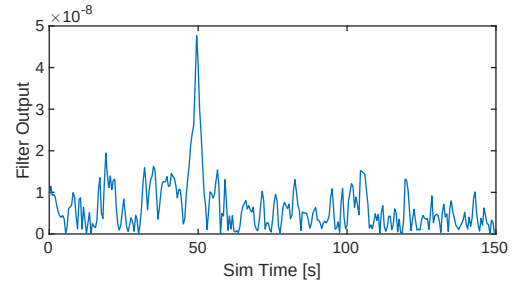

(c) Filter Output

Fig. 5: Example of matched filter accentuating a 50 mg debris strike applied at t=50 s. Note that when the strike is applied the telemetry increases slightly for a few points then decreases slightly, but it is difficult to see in the raw telemetry as it is beneath the noise floor. However, the filter produces a distinct spike in response.

vary linearly with $\frac{\phi}{2}$, where ϕ is the angle of the error in each axis.

3.2.2 Developing Filter Thresholds

The filter thresholds are developed using a Receiver Operating Characteristic (ROC) curve. To develop this curve, pdfs of the filter output are developed empirically. The first pdf is the filter output with no strikes present, to characterize the noise in the filter. Then a specified strike is applied to the simulation 1000 times and the filter response to each strike is logged and used to generate a pdf of filter response to that strike. The strike size is selected such that the center of the bell curve is in the vicinity of the desired threshold on the no-strike pdf. To achieve this, 30 mg strikes are applied to generate the filter response for attitude thresholds, and 40 mg strikes are applied to gen-

erate the filter response for rate thresholds. From the two pdfs the ROC curves are generated, and the slope of the ROC curve at P_{fa} = .01% corresponds to the threshold for the likelihood ratio test [18]. The likelihood ratio test is applied to possible filter outputs and the filter output at which the likelihood ratio test exceeds the threshold from the ROC curve is selected as the filter output threshold for strike detection. See Figure 2 for a graphical representation of this process.

3.2.3 Determining Strike Parameters

Once a debris strike is detected using the matched filter output and associated threshold, the task is to assess the magnitude of the debris strike. This is accomplished using a bank of matched filter wavelets and determining which filter wavelet shows the closest match to the telemetry. Then the size of strike used to generate that wavelet is selected as the estimated strike size.

Four methods are compared to determine which wavelet is closest to the telemetry. The first method takes the root-sum-squared error (RSSE) between the telemetry and each wavelet then selects the wavelet where this is a minimum. The second takes the minimum mean-squared error (MMSE), the third the minimum absolute error (MAE), and the fourth the sum of the absolute value of the error cubed ('Cubic'). The results show that the MMSE and RSSE have identical performance, which makes sense since the errors are penalized identically in both methods - as a function of the square of the error. The absolute error is penalized linearly while the fourth method penalizes the error cubed. Across 1000 Monte-Carlo runs with randomized debris strikes, the error in estimated strike magnitude for each method is shown in Table 2. Note that these errors are for accurately detected strikes only, Section 3.2.4 discusses the overall detection performance of the algorithm. Based on these results, the MMSE was selected as the estimation method for the remainder of this study. Figure 6 shows a wavelet bank, telemetry with the true state overlaid, and the results of each estimation method along with the true strike size.

Table 2: Comparing results of each estimation method

Estimation Method	Mean Error	Standard Dev.
Using Attitude		
MMSE	1.4 mg	8.7 mg
RSSE	1.4 mg	8.7 mg
MAE	2.0 mg	10.9 mg
Cubic	1.5 mg	9.1 mg
Using Rate		
MMSE	-4.46 mg	13.1 mg
RSSE	-4.46 mg	13.1 mg
MAE	-2.95 mg	14.3 mg
Cubic	-4.50 mg	13.2 mg

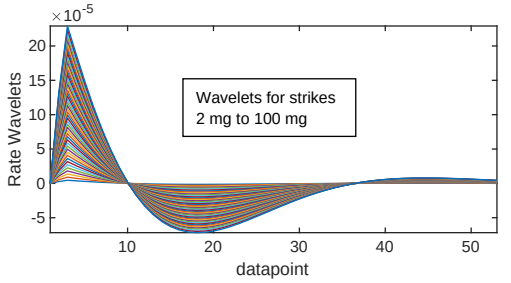

(a) Wavelet Bank

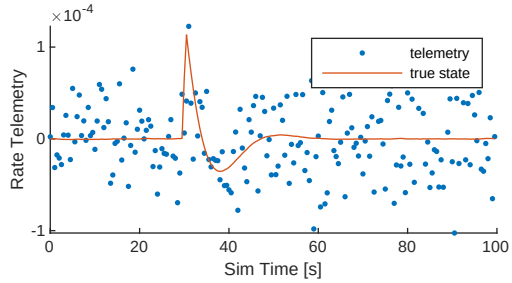

(b) Telemetry and True State

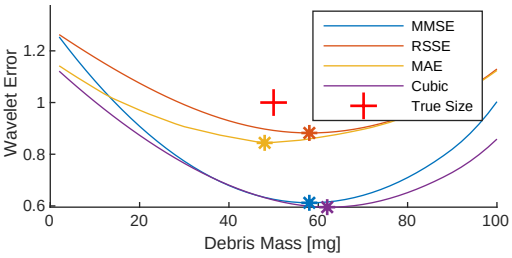

(c) Results from Estimators

Fig. 6: Wavelet bank and results from running filters against a 50 mg strike at t=30 s. Minimum error is selected as most probable strike size (58 mg). Results from each estimator are compared.

3.2.4 Assessing Algorithm Performance

To assess the algorithm's performance, a 1000 run Monte-Carlo is conducted randomizing the strike time, size, and direction. The enveloping matched filters from Section 3.2.1 are run against the telemetry to detect strikes per the thresholds developed in Section 3.2.2. When they detect a strike the wavelet bank is run at that time and the MMSE is computed. The closest-matching wavelet is selected as the strike's estimated size, and that result is compared to the true size. The results, shown in Figure 7, indicate that the attitude filter consistently detects strikes larger than 60 mg, while the rate filter consistently detects strikes larger than 80 mg. Both filters also detect smaller strikes, but the percentage detected decreases with smaller strikes. The estimated strike sizes cluster in the vicinity of the true strike sizes, but vary by around $\pm$ 20 mg. A fair number of outliers are under-predicted by more than that, especially via the rate telemetry.

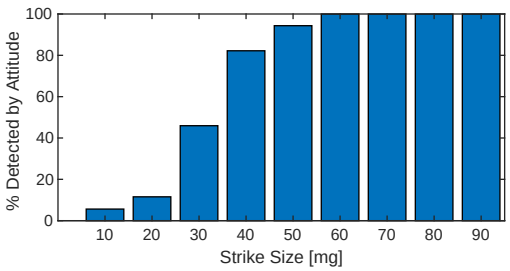

(a) Strikes Detected by Attitude Filters

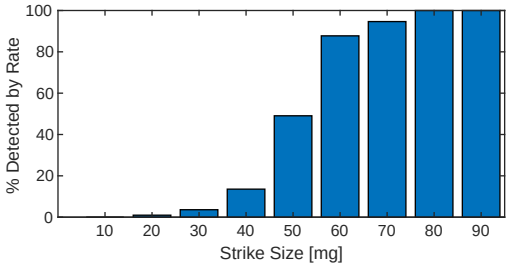

(b) Strikes Detected by Rate Filters

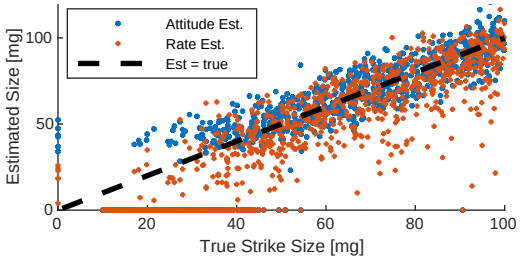

(c) True Size vs. Estimated Size

Fig. 7: Detection results per attitude matched filter and rate matched filter, and plot of estimated vs. true size. Non-detected strikes and false alarms shown as zeros on each axis.

3.3 Sequential Probability Ratio Tests (SPRTs)

Three SPRTs are implemented on the momentum telemetry, as the inertial momentum is fairly quiescent in the absence of external forces and a debris strike produces an abrupt change in momentum. SPRTs compare the noisy output data to an expected probability distribution and the filter output increases when a prolonged deviation from the expected output occurs. Since the momentum changes gradually due to effects like solar radiation pressure the parameters of the expected distribution change over time. To apply SPRTs to the debris strike problem a sliding window filter is used. This sliding window incorporates a 'pre-window' which is used to compute the expected distribution parameters, providing a fading estimate of the most recent distribution parameters. In the 'post-window' the SPRT algorithms are applied to detect changes from the distribution characterized in the pre-window. This causes the filters to peak at the debris strike time, when all data in the pre-window is before the strike and all data in the post-window is after the strike.

The simple summation filter subtracts the average of the pre-window from the post-window data and then sums the zeroed post-window data. When the mean of the post-window is similar to the mean of the pre-window the filter output, y_{sum}, is near zero. When a change occurred at the junction between the windows the filter output reaches a maximum. For m datapoints,

$$y_{\text{sum}} = \sum_{i=1}^{m} (x_i - \mu_{\text{pre-window}}) \tag{16}$$

The CUSUM algorithm sums the likelihood ratio of each datapoint given the μ and σ calculated from the pre-window compared to two alternative hypotheses: a displacement in $\Delta\mu$ N.m.s in either the positive or negative direction. Then the test statistic W_n from Equation (11) is used as the filter output. This also produces a maximum at approximately the time of the strike.

The Shiryaev algorithm applies the recursive relation in Equation (13) to each data point for j alternative hypotheses, where each $\mathcal{H}_j$ is a displacement of $\boldsymbol{n}\Delta\mu$ N.m.s from the μ of the pre-window and $\boldsymbol{n}$ is a 1D array of integers from -10 to 10. The final CDFs ($F_{j,\text{end}}$) at the end of the post window are used as a weights to produce the following weighted sum as the estimated change in μ based on the entire post-window measurement sequence

$$\Delta\mu_{\text{est}} = \sum_{i=1}^{j} n_i \Delta\mu F_{i,\text{end}} \tag{17}$$

3.3.1 Tuning Filter Parameters

The performance of each of the SPRTs is dependent on the filter parameters such as the length of the post-window and the choice of $\Delta\mu$. The length of the pre-window is fixed at 200 datapoints to allow reasonable computation times, and $\tilde{p}$ for the Shiryaev algorithm is fixed at 1×10^{-6}.

To determine appropriate filter parameters for this study the performance of the filters is characterized while trading the length of the post-window and the magnitude of $\Delta\mu$. The desire is to maximize the SNR while maintaining the ability to detect small strikes. Figure 8 shows the CUSUM and Shiryaev filter output from 5, 10, and 20 mg strikes while trading the post-window length and $\Delta\mu$ The mean of the peak at the strike time is divided by three times the standard deviation of the filter noise when no strikes are present ($\mu_{\text{strike}}/3\sigma_{\text{no strike}}$).

The results from the summation filter are not included in the graphic because they increase consistently with increasing post-window length and are unaffected by $\Delta\mu$. Therefore, the choice of filter parameters is easy: the largest post-window practical should be used. The length

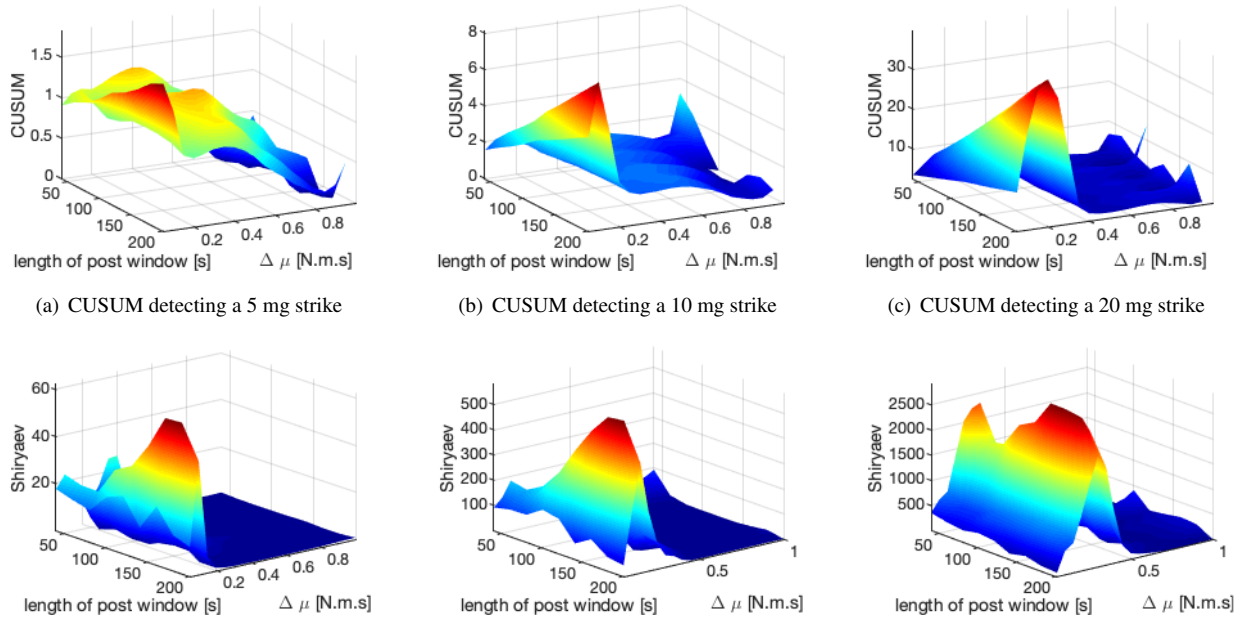

(a) CUSUM detecting a 5 mg strike

(b) CUSUM detecting a 10 mg strike

(c) CUSUM detecting a 20 mg strike

(d) Shiryaev detecting a 5 mg strike

(e) Shiryaev detecting a 10 mg strike

(f) Shiryaev detecting a 20 mg strike

Fig. 8: The filter parameters are traded and the SNR of the resultant filter output plotted to identify optimum filter parameters. The CUSUM algorithm shows a peak in SNR with long post-windows and small $\Delta\mu$s The $\Delta\mu$ which shows the best SNR increases with increasing strike size. The Shiryaev algorithm shows similar behavior with increasing $\Delta\mu$ but the trend with increasing window length is less consistent. The Shiryaev algorithm's noise is highly non-Gaussian, which may contribute to this inconsistency.

of the post-window is limited by computational time for this study, as the strikes must be spaced apart enough that the filter never reaches two strikes simultaneously. In real-world telemetry, the maximum length of the filter is determined by the rate of change in momentum. The filter should be run on a set of data where the average remains the same relative to the magnitude of the debris strikes that are being detected.

A post-window of 180 datapoints is chosen for this study as this allows reasonable computation time for long Monte-Carlo runs. This is also the peak of the Shiryaev SNR. A $\Delta\mu$ of 0.1 N.m.s is chosen for the CUSUM algorithm, which is the peak of the SNR for detecting a 10 mg strike and not too far below the peak for 5 mg and 20 mg strikes. Strikes larger than this have a peak at a higher $\Delta\mu$, but they are also easier to detect. For the Shiryaev the $\Delta\mu$ of the peak also increases with increasing strike size. However, since the Shiryaev algorithm estimates the strike size according to the discrete intervals defined by the $\Delta\mu$ array, it is not ideal to pick the $\Delta\mu$ with the maximum SNR as that would result in only strikes of that size or larger being detectable. Therefore, the Shiryaev $\Delta\mu$ array is chosen to achieve the desired granularity in strike size estimates. A granularity of 5 mg in strike size corresponds to a $\Delta\mu$ of .04 N.m.s, so that is selected as the $\Delta\mu$ for the Shiryaev algorithm. As indicated on the Z-axis of Figure 8(d-f), this still provides a satisfactory SNR.

With these parameters, the filters produce the results shown in Figure 9 when strikes with magnitudes 5, 10, 15, and 20 mg are applied in the x-axis. As shown, the filters struggle to detect the 5 mg strike as the output is close to the noise floor, but the 10 mg strike and higher are clear. The CUSUM algorithm and summation filter both show peaks at approximately the time of the strike, but the Shiryaev algorithm tends to have a long plateau in the vicinity of the strike. This is because this algorithm is developed to provide quick change detection, so as soon as the end of the post window starts incorporating the change the algorithm begins predicting that the change has occurred, then the estimates for the change are refined, becoming less noisy as more of the post-window includes the change. Eventually the window passes the point of the change, then the estimates for the change drop off as the pre-window starts incorporating the change in its fading assessment of the $\mathcal{H}_o$ parameters. Note that the simple summation algorithm has a noticeable peak for the smallest strike, while the CUSUM does not because it is below its detection threshold. However, the CUSUM has an excellent SNR for the three larger strikes.

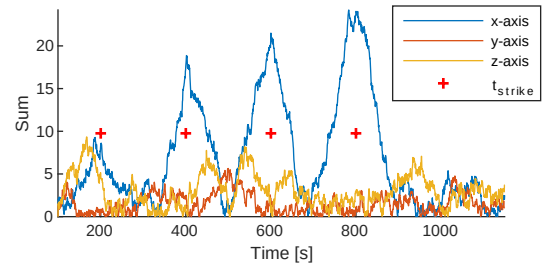

(a) Output of simple summation filter

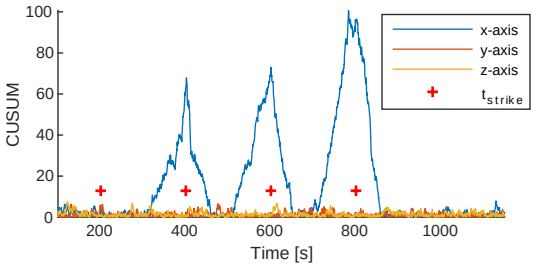

(b) Output of CUSUM filter

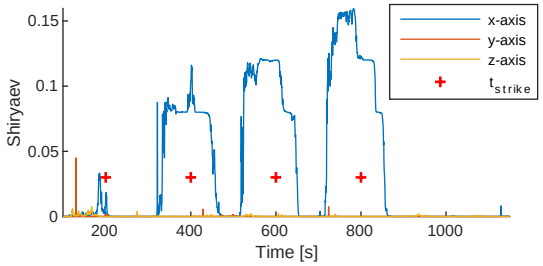

(c) Output of Shiryaev filter

Fig. 9: Output of SPRT filters with 5, 10, 15, and 20 mg strikes applied to the x-axis

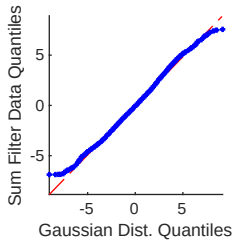

(a) Sum, No Strikes

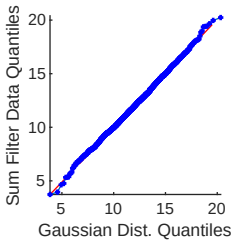

(b) Sum, 10 mg Strikes

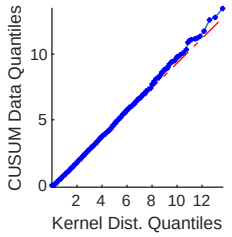

(c) CUSUM, No Strikes

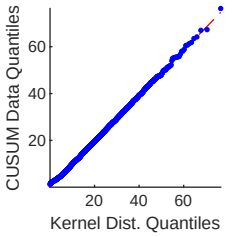

(d) CUSUM, 10 mg Strikes

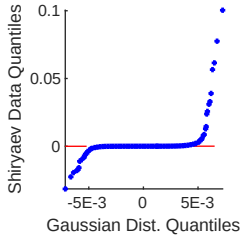

(e) Shiryaev, No Strikes

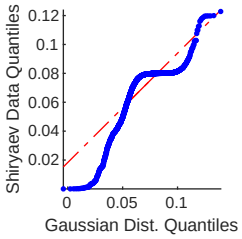

(f) Shiryaev, 10 mg Strikes

Fig. 10: Q-Q plots illustrating results when fitting various distributions to filter output

3.3.2 Developing Filter Thresholds

To develop detection thresholds the pdf of filter output is used, similar to Section 3.2.2. However, the filter output for the SPRT filters is not always Gaussian like the matched filter output, so each algorithm's threshold development is tailored to accommodate its own unique output distribution parameters. The noise distribution for the output of each algorithm when no debris strikes are present is developed using a simulation with 40,000 filtered datapoints, while the noise distribution for the output when a strike is present is developed by applying a 10 mg strike to the simulation 1,000 times and measuring the peak response. Figure 10 shows the Q-Q plots of the filtered data using distributions specific to each algorithm.

Summation Filter Output Distributions

The output of the summation filter with no debris strikes is modeled fairly well by a Gaussian distribution. The filter's output has slightly lighter tails than a Gaussian distribution, so the thresholds developed using a Gaussian are somewhat conservative in terms of false alarm rate. The peak of the filter output when a debris strike is applied is also fairly Gaussian, so the method outlined in Section 2.2 is used to develop thresholds for strike detection using a desired P_{fa} of 0.01%. Based on the ROC curve, the selected threshold for the summation filter is 8.8.

CUSUM Output Distributions

The CUSUM algorithm has a one-sided output and thus requires a one-sided pdf. However, standard one-sided pdfs have lighter tails than the data from the CUSUM algorithm producing more false alarms than desired. To avoid this, a kernel distribution is used. When a debris strike is present the variation in the peak of the CUSUM algorithm is two-sided but skewed, so a kernel distribution is also used for that model. The pdfs generated by these distributions are used to develop the detection thresholds for the CUSUM algorithm per Section 2.2. This results in a threshold of 13.4 for the CUSUM algorithm. Note that 10 mg is slightly below the size of strike that the CUSUM algorithm is tuned to detect, so the output is variable resulting in a broad pdf.

Shiryaev Output Distributions

The Shiryaev algorithm's output is highly non-normal and defied all attempts to model it with standard pdfs. This applies to both the no-strike noise parameters and the output during debris strikes. Therefore, instead of using a poorly-fitted and non-representative ROC curve the thresholds are developed empirically from the no-strike noise data. Based on this data, a threshold of 0.03 N.m.s, or 75% of the smallest strike the algorithm is tuned to detect is selected. This threshold produced a P_{FA} of 0.4% in one long simulation, but the threshold's true P_{FA} is not assessed analytically due to the lack of accurate pdfs characterizing the data.

3.3.3 Assessing Detection Performance

A 1,000-run Monte-Carlo is conducted to assess each algorithm's ability to detect debris strikes using the thresholds developed in Section 3.3.2. The Monte-Carlo randomizes the strike magnitude and direction, so it is applied on any combination of the three axes. Figure 11 shows the detection accuracy of each algorithm for various strike sizes. These results indicate that detection performance is excellent for all three algorithms for strikes greater than 10 mg. Note that strike direction is randomized as well as strike magnitude, so each axis sees only a fraction of each strike.

The detection results for the CUSUM algorithm taper off more quickly than the Shiryaev or summation filter results, but this is likely due to the filter being tuned to detect strikes slightly larger than 10 mg. If the filter were tuned to detect smaller strikes it would likely perform a little better, as the SNR is exemplary as shown in Figure 9. However, the filter output noise would increase if it were tuned to detect smaller strikes so the current tuning is maintained as a conservative and reliable filter.

The Shiryaev and summation filters show an ability to detect some strikes even in the < 3 mg range. It is possible that some of these strikes are false alarms. In a run with no strikes and 20,000 datapoints the Shiryaev filter produced eight false alarms while the summation filter produced one and the CUSUM filter produced zero. In a run the length of this Monte-Carlo simulation there would likely be well over 100 false alarms for Shiryaev and a dozen or so for the summation filter, although many of those would be hidden within the response to real strikes.

3.3.4 Estimating Strike Parameters

When a strike is detected by the simple cumulative sum filter or the CUSUM algorithm an estimate of strike parameters is obtained by comparing the average of the pre-window data to the average of the post-window data for each axis. The difference in averages is used as an estimate of the momentum imparted by the strike. With the Shiryaev algorithm's weighted sum the output of the filter

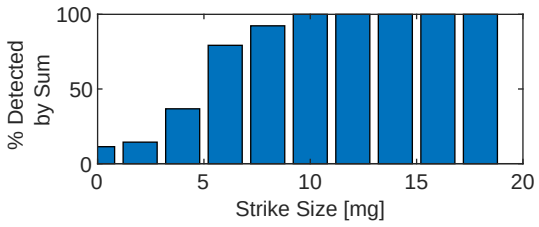

(a) Detection performance of simple summation filter

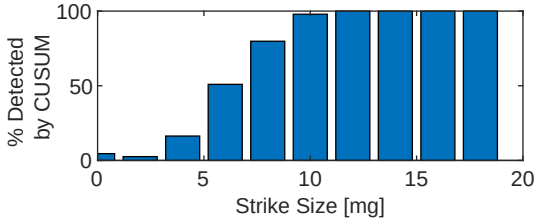

(b) Detection performance of CUSUM filter

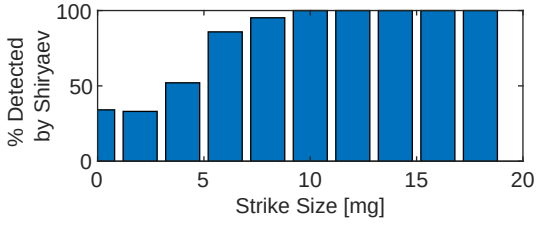

(c) Detection performance of Shiryaev filter

Fig. 11: Detection performance of each filter on 1,000 randomized strikes

corresponds to the estimated strike size, so the filter output is used as an estimate of strike parameters. Figure 12 shows the accuracy of each filter in estimating strike magnitude by plotting the true vs. estimated strike size. Non-detected strikes are shown on the x-axis. These results show that both methods do an exemplary job of estimating strike parameters. The estimates from the Sum and CUSUM algorithms tend to be more accurate, with nearly all the errors within ± 5 mg. The results from the Shiryaev algorithm are good as well but have significantly more outliers with poor estimates.

4. Results

The matched filters perform well for detecting strikes larger than about 40 mg, and can estimate the strike size to within around $\pm$ 20 mg. Matched filters offer the advantage of Gaussian filter output which allows high confidence in the filter's false alarm rate. This is key when these methods are used to evaluate debris populations using on-orbit telemetry, since the level of confidence in the results must be understood to evaluate whether the measured strikes are reasonable based on the modeled fluxes.

The performance of the SPRT methods run against the inertial angular momentum telemetry is outstanding. They are able to detect debris strikes reliably down to 10

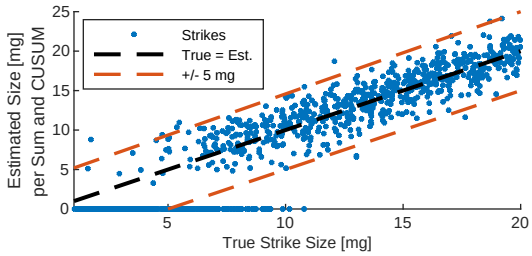

(a) Estimation performance of CUSUM and summation filters

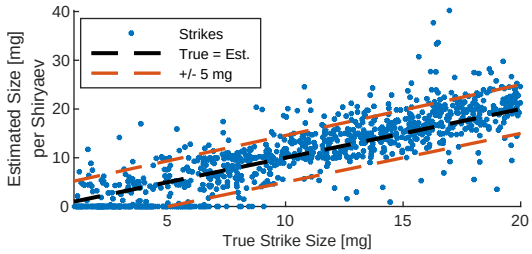

(b) Estimation performance of Shiryaev filter

Fig. 12: True size of each strike in 1,000 run Monte-Carlo compared to estimated size using two estimation methods

mg and occasionally down to 3 mg or less. Their estimation performance is also excellent, generally estimating strike magnitudes to within ± 5 mg. This is especially significant because the momentum telemetry is calculated from the noisy attitude and rate telemetry as well as noisy wheel speed telemetry. This shows that the SPRT algorithms' ability to identify subtle changes in noisy telemetry is exceptional.

Each SPRT algorithm has unique strengths and weaknesses. The summation algorithm offers extremely low computational requirements, and very little tuning or *a priori* knowledge is required to run it effectively. Its noise parameters are also fairly well modeled which allows the selection of thresholds with predictable false alarm rates. However, it has the highest SNR of any of the algorithms which may degrade its performance on orbit when the measurement and state noise is not necessarily Gaussian.

The CUSUM algorithm offers consistent performance and a very low SNR, with noise parameters that, while not Gaussian, did allow modeling via kernel distributions. Drawbacks are that it requires design choices about the size of strike to detect and that it has a non-trivial computational burden as the likelihood ratios must be computed for every datapoint in every sliding window. However, for running on telemetry as it is downlinked or running on historical telemetry it performs very well.

The Shiryaev algorithm is challenging in its highly non-Gaussian distribution parameters which make it difficult to assess the false alarm rate for a given threshold. It has very good performance but is more finicky than the CUSUM algorithm, and it is difficult to determine the time of the strike with reasonable accuracy. This could be a detractor if trying to identify the effects of the strike in multiple telemetry streams.

5. Discussion

5.1 Dependency of Results on Study Parameters

All these results are highly dependent on the noise applied to the telemetry, and are also dependent on the spacecraft design parameters. The noise values are loosely derived from noise seen in on-orbit telemetry from NASA's Solar Dynamics Observatory, but analysis and simulation of a specific spacecraft would have to be performed to determine a particular spacecraft's capabilities for accurately detecting and identifying debris strikes. Also, this study uses the perfect simulation parameters when calculating momentum and matched filter wavelets. In reality, there will be discrepancies between the as-designed parameters and the as-built parameters, and the effects of those discrepancies should be characterized.

5.2 Comments on False Alarms

Note that increasing the probability of detection necessarily increases the probability of false alarm by moving the threshold (see Figure 2(a)). For this analysis thresholds were selected which made the P_{FA} very low compared to the P_D. Additional strikes could be detected by lowering the thresholds, but the resultant increase in false alarms would have to be taken into account when comparing the results to predictions from debris models.

5.3 Potential Application: Buffering and Downlinking Strike Telemetry

The state data from the simulation is truncated to 2 Hz to represent downlinked telemetry. Obtaining data at a higher rate would likely improve the ability to detect and estimate small debris strikes, but bandwidth limitations typically result in only necessary state of health telemetry being downlinked. This results in telemetry that is at a much lower rate than is processed on-board. Since the summation algorithm is computationally simple it could easily be run on-board. Potentially, telemetry could be buffered on-board and then downlinked at a higher rate if a probable strike is detected. The higher rate telemetry could be analyzed with the computationally intensive algorithms and the transient effects on other systems could be observed in higher rate telemetry when they might be missed in the standard low-rate telemetry.

5.4 Challenges in Application to Real-Word Telemetry

Applying these techniques to on-orbit telemetry is a non-trivial challenge, as the noise and events experienced by a real spacecraft tend to trip the debris detection algorithm thresholds frequently even when no strike is present. While the theoretical inertial momentum is perfectly quiescent in the absence of external forces, the reality is

more variable than expected. For example, NASA's Solar Dynamics Observatory sees a cyclical abrupt change in its momentum approximately every 13 minutes, which is consistent across years of data. This cyclical change must be filtered out so that 'debris strikes' are not detected every 13 minutes. Station-keeping maneuvers and scanning maneuvers also trip the strike detection thresholds, so each spacecraft requires its own suite of algorithms to detect events that cause fluctuations in the calculated momentum and mask the filter output during these events. In addition to on-board events, solar radiation pressure and space weather effects can influence the spacecraft's telemetry and manifest as debris strikes.

For example, Bogorad showed that an electrostatic discharge (ESD) event can impart momentum to the discharging object [21]. The abrupt momentum transfer would be interpreted as a debris strike using these algorithms. This is especially difficult to mitigate as a hypervelocity impact can also create an ESD event, so differentiating an ESD event that causes momentum transfer from a debris strike that causes ESD is a unique challenge.

Another consideration is that, since debris strikes occur rarely, significant quantities of data must be processed to detect them. This requires a data-processing architecture that is computationally efficient and capable of autonomously processing far more data than many applications can accommodate, necessitating 'big data' methods.

The fun doesn't end when a debris strike is detected and the parameters are estimated. As discussed in Section 2.1, the momentum imparted by the debris to the spacecraft is only a fraction of the momentum of the debris relative to the spacecraft if the impactor breaks through. However, if the impactor is stopped by the structure the plume of ejecta causes the imparted angular momentum to exceed the relative momentum of the debris by a factor of two or more. This highlights the importance of examining other telemetry, such as solar array power output, for indicators of the strike. If the strike's location can be identified it improves the ability to determine whether the estimated strike parameters are overpredicting or underpredicting the actual relative momentum of the debris. It is important to note that the methods developed in this paper only return the angular momentum of the strike, so a small and fast micrometeoroid could manifest similarly to a slower and larger piece of orbit debris.

5.5 Future Work

An ongoing study is assessing the telemetry of several of NASA's space science missions for debris strikes. Applying these methods to on-orbit telemetry is a critical element in their successful development, since the noise and events in on-orbit telemetry make it significantly more difficult to process than simulated telemetry with perfect Gaussian noise.

Another critical element of this development is to determine the effects that the noise parameters and spacecraft parameters have on the filter's ability to identify and assess strikes. Each spacecraft typically has a unique instrument suite, and will therefore have unique noise and response characteristics. This study shows a single design point, and that must be extended in a trade study to understand different spacecrafts' abilities to accurately identify and assess strikes. The filters need to be tuned for each spacecraft based on the noise characteristics of the filter output for that spacecraft.

In the Sentinel-1A debris strike (Figure 1) the spacecraft rate telemetry exhibited a significant amount of 'ringing' which was probably due to the fundamental frequency of the solar array being excited by the strike. A similar phenomenon was observed in the MMS strikes. This might obfuscate the effects of the strike as the calculated spacecraft momentum would probably also 'ring' instead of showing an abrupt change and this would have an effect on the SPRT algorithms' output. However, the ringing itself might also provide an effect that could be detected with the right filter. These real-world strikes show that this study's assumption of a rigid body spacecraft is not entirely accurate for debris strikes on appendages. A spring-mass-damper appendage can be added to the simulation for assessment in a future study.

An essential element of validating the data returned by these methods is to compare the strikes predicted via debris models to detected strikes. This model comparison should take into account micrometeoroid populations as well as debris, and the effects of the time-variance of flux density throughout the orbit, i.e. polar regions exhibiting higher debris fluxes for LEO spacecraft and 'rush hours' for GEO spacecraft [22].

Additional telemetry types should be considered for their contributions to identifying and assessing debris strikes. In particular, if a debris strike is large enough to change the orbit measurably the linear momentum can be estimated, which can be combined with the angular momentum to estimate the strike location on the spacecraft.

If a significant population of debris strikes is produced from on-orbit telemetry then machine learning algorithms can be developed using those strikes as a training population. Machine learning algorithms are of interest for their ability to not only detect debris strikes in ACS telemetry but also find subtle indicators of strikes in other telemetry types, such as solar array power or thermal profiles.

6. Conclusions

This study develops practical and effective methods for identifying subtle debris strikes using standard spacecraft telemetry. It provides an innovative tool for spacecraft operators to gain insight into the debris environment for their spacecraft's orbit. This additional insight will be critical

to enable the increasing use of all Earth orbits by burgeoning populations of space objects. Over 90% of the debris that can harm a spacecraft is untrackable and accurately modeling these populations is challenging, especially for higher orbits. Leveraging active satellites as *in situ* debris sensors with inherent ability to detect minor strikes would revolutionize the space industry's understanding of the untrackable debris environment to improve debris modeling, anomaly attribution and response, and debris risk assessments for future missions.

Acknowledgements

This work was supported by a NASA Space Technology Research Fellowship.

References

[1] "Monthly Number of Objects in Earth Orbit by Object Type". In: *Orbital Debris Quarterly News* Volume 23.1 (May 2019).

[2] James Shell. "Optimizing orbital debris monitoring with optical telescopes". In: Advanced Maui Optical and Space Surveillance Technologies Conference. Maui, HI, Sept. 14, 2010.

[3] Michael Squire. "Micrometeoroid and Orbital Debris Testing on Composite Overwrapped Pressure Vessels". 2019 Applied Space Environments Conference. Los Angeles, CA, May 15, 2019.

[4] E. Christiansen et al. "Reaction of Spacecraft Batteries to Hypervelocity Impact". In: *Orbital Debris Quarterly News* 21.1 (Feb. 2017).

[5] *Space Debris by the Numbers*. European Space Agency. https://www.esa.int/Our_Activities/Space_Safety/Space_Debris/Space_debris_by_the_numbers, (accessed 8-6-19).

[6] *Evaluation of Micrometeoroid and Orbital Debris (MMOD) Risk Predictions with Available Onorbit Assets*. NASA Engineering and Safety Center Technical Assessment Report NESC-RP- 14-01000. NASA Engineering and Safety Center, Oct. 13, 2017.

[7] H. Krag et al. "A 1 cm space debris impact onto the Sentinel-1A solar array". In: *Acta Astronautica* 137 (Aug. 2017), pp. 434–443.

[8] Stephen Clark. "Investigators conclude external forces killed an Intelsat satellite in April". In: *Spaceflight Now* (July 30, 2019).

[9] Trevor Williams, Joseph Sedlak, and Seth Shulman. "Magnetospheric Multiscale Mission Micrometeoroid/Orbital Debris Impacts". In: Spacecraft Anomalies and Failures Workshop 2017. Chantilly, VA, Dec. 12, 2017.

[10] Donald Humes. *Large Craters on the Meteoroid and Space Debris Impact Experiment*. N92-23309. NASA Langley Research Center.

[11] G.A. Graham et al. "The chemistry of micrometeoroid and space debris remnants captured on hubble space telescope solar cells". In: *International Journal of Impact Engineering* 26.1 (Dec. 2001), pp. 263–274.

[12] A.J Tuzzolino et al. "The Space Dust (SPADUS) instrument aboard the Earth-orbiting (ARGOS) spacecraft". In: *Planetary and Space Science* 49.7 (June 2001), pp. 689–703.

[13] Waldemar Bauer, Oliver Romberg, and Robin Putzar. "Experimental verification of an innovative debris detector". In: *Acta Astronautica* 117 (Dec. 2015), pp. 49–54.

[14] Ingrid Mann et al. "Dust observations with antenna measurements and its prospects for observations with Parker Solar Probe and Solar Orbiter". In: *Annales Geophysicae Discussions* (July 15, 2019), pp. 1–39.

[15] Brien Flewelling et al. "Explained and Unexplained Momentum Impulse Transfer Events". In: 7th European Conference on Space Debris. Darmstadt, Germany: ESA Space Debris Office, Apr. 18, 2017.

[16] Hanspeter Schaub and John L. Junkins. *Analytical mechanics of space systems*. Third edition. AIAA education series. Reston, Virginia: American Institute of Aeronautics and Astronautics, Inc, 2014.

[17] Pierre Moulin and Venugopal V. Veeravalli. *Statistical inference for engineers and data scientists*. Cambridge, UK ; New York, NY: Cambridge University Press, 2019.

[18] Bernard C. Levy. *Principles of signal detection and parameter estimation*. New York, NY: Springer, 2008.

[19] Durga P Malladi and Jason L Speyer. "A Generalized Shiryayev Sequential Probability Ratio Test for Change Detection and Isolation". In: *IEEE Transactions on Automatic Control* 44.8 (1999), p. 13.

[20] Joel Williamsen and Steven Evans. "Orbital debris momentum transfer in satellite shields following hypervelocity impact, and its application to environment validation". In: *Procedia Engineering* 204 (2017), pp. 500–507.

[21] Alexander L. Bogorad et al. "Electrostatic Discharge Induced Momentum Impulse From Charged Spacecraft Surfaces". In: *IEEE Transactions on Nuclear Science* 53.6 (Dec. 2006), pp. 3607–3609.

[22] Darren S. McKnight and Frank R. Di Pentino. "New insights on the orbital debris collision hazard at GEO". In: *Acta Astronautica* 85 (Apr. 2013), pp. 73–82.